J. Hydrol. Hydromech., 73, 2025, 4, 443–456
https://doi.org/10.2478/johh-2025-0033

Journal of Hydrology and Hydromechanics

Flow past one and two adjacent square cylinders based on a two-fluid turbulence model

Murodil Madaliev, Zokhidjon Abdulkhaev*, Mumin Nabiev, Abdurakhim Dustmatov

Fergana State Technical University, Fergana, Uzbekistan, 150100.
* Corresponding author. E-mail: zokhidjon@fstu.uz

Abstract: This paper presents an improved version of the Spalding two-fluid turbulence model developed by Malikov. The model is applied to numerically simulate turbulent flows past one and two square cylinders at a Reynolds number of Re = 47,000. The SIMPLE algorithm with a semi-implicit scheme and second-order accuracy is used to solve the equations. The code developed by the authors was tested on a two-dimensional benchmark problem of flow past a single square cylinder and then applied to crossflow past two square cylinders located side by side. The ratio of the distance between the cylinders, T/d, varied from 0 to 5, which allowed us to identify three characteristic flow regimes: single, slot (interference), and antiphase synchronous. The simulation results were compared with experimental data and showed good agreement in terms of pressure distribution, vortex wake structure, and aerodynamic force coefficients. Comparison with RANS and LES models confirmed that Malikov's model provides comparable accuracy with significantly lower computational costs.

Keywords: Navier–Stokes equations; Separated flow; Control volume method; Two-fluid model; SIMPLE algorithm.

1 INTRODUCTION

Cylindrical engineering structures are often located in groups—in buildings, pipelines, bridges, and other objects. Therefore, it is important to consider the aerodynamic interactions between them. The basic model for such a configuration is two cylinders placed side by side, which demonstrate key flow properties: flow separation, vortex formation, recirculation, and shear layer interaction (Huang and Li, 2010; Lim et al., 2009; Nozawa and Tamura, 2002; Shimada and Ishihara, 2002).

Flow around a single circular cylinder has been extensively studied in recent decades and has served as the basis for understanding the fundamental properties of turbulent flows. Unlike a circular cylinder, flow separation in a square cylinder occurs at fixed sharp edges, which alters the wake structure. The square cylinder configuration at Re = 22000 and 0° angle of attack is often used as a benchmark for testing turbulent models (Bao et al., 2011; Sohankar et al., 2000).

When two square cylinders are located adjacent to each other, the flow becomes significantly more complex and depends not only on the Reynolds number but also on the distance between the cylinders. Despite this, such configurations have been studied significantly less. Previous studies (Alam et al., 2011; Inoue et al., 2006; Yen and Liu, 2011 and Kolář et al., 1997) demonstrate the existence of three flow regimes (single, slot, and paired vortex), as well as the influence of distance on the drag coefficients and vortex shedding frequency.

Two approaches are used to study turbulent flows: experimental and numerical. The latter is preferred due to its lower cost and flexibility. Among numerical methods, DNS provides high accuracy but requires extremely high grid resolution ($Re^{9/4}$), making it resource-intensive.

Large eddy simulation (LES) is less expensive and has been successfully applied to unsteady problems (Afgan et al., 2011; Li and Ahmadi, 1992; Raissi et al., 2017; Tian and Ahmadi, 2007; Zhang et al., 2001; Zou et al., 2008), but at high Re it also requires significant resources, especially in the wall regions.

An alternative is the RANS approach, which allows for the computation of flows at high Re at a lower cost. For example, the k–ε (Shimada and Ishihara, 2002) and Spalart–Allmaras (SA) (Huang and Li, 2010; Spalart and Allmaras, 1992) models are widely used in engineering practice. The one-equation SA model is particularly effective due to its simplicity and low computational expense, but like other RANS models it can yield weak results in problems with separation, recirculation, and complex anisotropy.

A comparison of RANS models for flow past a square cylinder was conducted by (Haque et al., 2013), and in (Rusdin, 2017), it was noted that the Reynolds stress model (RSM) predicts the most accurate longitudinal velocity profile, although it performs worse in estimating the turbulent stresses.

One alternative approach to RANS turbulence modeling is the Spalding two-fluid model (Spalding, 1983), based on the separation of the flow into two fluids with different physical properties. Initially, the model divided the flow into "turbulent" and "non-turbulent" (Andrews, 1986; Markatos and Kotsifaki, 1994; Spalding and Malin, 1984), then into "fast" and "slow" fluids with symmetric mass transfer(Spalding, 1985). Based on Prandtl's hypothesis, a formula for turbulent viscosity was derived. Despite successful applications, the model requires twice as many equations as RANS, which limits its use in engineering problems. The development and expansion of the application of the two-fluid model has been noted in many studies: for stratified flows (Shen et al., 2003), convective heat transfer in air curtains (Yu et al., 2008), UV disinfection reactors (Liu et al., 2007), and for the analysis of Rayleigh-Taylor mixing (Youngs, 1996). A comprehensive historical review and discussion of Spalding's contribution to turbulent flow modeling are provided by (Fueyo and Malin,2020).

In recent works by Malikov and co-authors (Alam et al., 2011; Malikov, 2020; Malikov, 2021, 2022; Z. Malikov et al., 2024; Z. Malikov and Madaliev, 2020, 2022), a new two-fluid turbulence model was developed based on the first Reynolds hypothesis, where the flow is considered as a mixture of two fluids moving relative to each other. This model was successfully applied to heattransfer problems (Malikov, 2021), multicomponent compressible flows (Malikov, 2022) and confirmed by verification on problems from the NASA database. Its advantages include ease of implementation, high accuracy, and robustness in modeling anisotropic turbulence. For example, it has shown good results in calculating an air centrifugal separator (Malikov and Madaliev, 2020). A detailed review of alternative turbulence models is omitted here, since it has already been presented in (Alam et al., 2011; Malikov, 2020, 2021, 2022; Malikov et al., 2024; Malikov and Madaliev, 2020, 2022). Instead, we focus on validating the new model for flow past two adjacent square cylinders, which has rarely been studied in the literature. In a previous study (Malikov and Madaliev, 2022), a two-fluid turbulence model was successfully applied to simulate separated flow past a single square cylinder, confirming its ability to accurately describe the key characteristics of vortex formation and pressure distribution in the wake zone. This study builds on that work and aims to expand the model's applicability to a more complex aerodynamic configuration, two adjacent square cylinders. In this case, the problem is significantly complicated by the intense interaction between vortex streets, which alters the flow structure, vortex separation dynamics, and aerodynamic load distribution. The analysis performed not only validates the versatility of Malikov's model but also evaluates its effectiveness in describing mutual interference effects that arise in flow past multiple bodies.

Some preliminary results were presented at a conference (Madaliev et al., 2025). In that paper, we considered two square cylinders arranged with spacings of T/d=2.4, 3.5, and 5, for which the interaction of the Karman vortex streets between the cylinders is minimal, and virtually independent wake formation is observed behind each cylinder. In contrast, the present study focuses on zones where vortex structures actively interact, i.e., with closer cylinder configurations, leading to increased mutual influence of their turbulent wakes. This allowed us to more thoroughly analyze the flow physics under conditions of strong aerodynamic interaction and identify characteristic features of vortex formation, which are inaccessible at large intercylinder spacings. The present paper contains a more comprehensive numerical validation with a detailed comparison with experimental data (Alam et al., 2011), which constitutes its maincontribution to the literature. The objective of this study is to validate a recently developed two-fluid turbulence model for solving the problem of separated flow past two adjacent square cylinders at a Reynolds number of Re = 47,000. For this purpose, numerical results are compared with reliable experimental data (Alam et al., 2011), which allows us to evaluate the accuracy and applicability of the model under conditions of intense interaction of vortex structures between bodies.

2 MATHEMATICAL MODEL

2.1 Theoretical foundations and derivation of Malikov's two-fluid model

The development of two-fluid approaches to describing turbulence dates back to the Spalding model (1983), which considered the flow as a mixture of two fluids, one turbulent and one non-turbulent, exchanging mass and momentum. However, the Spalding model did not clearly define the physical nature of flow separation, which limited its application. Furthermore, the use of two sets of continuum equations and an additional equation for the fragment size (Prandtl's mixing length) significantly increased computational costs and complicated implementation. In contrast, the new two-fluid model of Malikov (2020–2022) relies on the first Reynolds hypothesis and provides a physically sound representation of turbulent flow as an inhomogeneous mixture of two interpenetrating fluids—one fast and one slow—moving relative to each other. In this approach, turbulent pulsations are interpreted not as mathematical deviations, but as the result of real relative displacements of fluid volumes at different velocities.

Let ΔS_i be the elementary flow area through which two volumes of liquids move with velocities V_{1i}, V_{2i}, occupying fractions α_1 and α_2, respectively ($\alpha_1 + \alpha_2 = 1$). Then the average velocity of the mixture is determined by the expression:

$$V = \alpha_1 V_1 + \alpha_2 V_2. \quad (1)$$

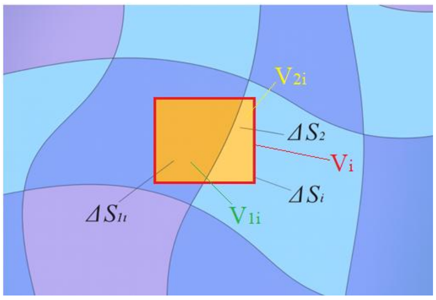

Fig. 1. Schematic representation of the flow of two liquids.

The pulsating nature of the turbulent flow is explained by the change in surface fractions α_i over time. These quantities fluctuate and describe the mixing of regions at different speeds.

Therefore, the velocity of a turbulent flow can be represented as the sum of the average $\bar{V}_i$ and pulsating ϑ_i' velocities:

$$V_i = \bar{V}_i + \vartheta_i'. \quad (2)$$

Thus, representing a turbulent flow as a mixture of two flows, we write the equations of continuity and motion for each fluid in the form

$$\begin{gathered}
\frac{\partial \varepsilon\rho}{\partial t} + \frac{\partial \rho\alpha_j V_{1j}}{\partial x_j} = J, \frac{\partial(1-\varepsilon)\rho}{\partial t} + \frac{\partial \rho(1-\alpha_j)V_{2j}}{\partial x_j} = -J, \\
\frac{\partial \varepsilon\rho V_{1i}}{\partial t} + \frac{\partial \alpha_j(\rho V_{1j}V_{1i} + \delta_{ij}p - \sigma_{1ji})}{\partial x_j} = f_i, \\
\frac{\partial(1-\varepsilon)\rho V_{2i}}{\partial t} + \frac{\partial(1-\alpha_j)(\rho V_{2j}V_{2i} + \delta_{ij}p - \sigma_{2ji})}{\partial x_j} = -f_i, \\
\sigma_{1ij} = \mu\left(\frac{\partial V_{1i}}{\partial x_j} + \frac{\partial V_{1j}}{\partial x_i}\right), \sigma_{2ij} = \mu\left(\frac{\partial V_{2i}}{\partial x_j} + \frac{\partial V_{2j}}{\partial x_i}\right).
\end{gathered} \quad (3)$$

Here J is the mass transfer intensity; f_i is the interaction force between the liquids, and μ is the dynamic viscosity coefficient of the liquid. In system (3), we perform averaging and obtain the system

$$\begin{cases}
\frac{\partial 0.5\rho}{\partial t} + \frac{\partial 0.5\rho V_{1j}}{\partial x_j} = \bar{J}, \\
\frac{\partial 0.5\rho}{\partial t} + \frac{\partial 0.5\rho V_{2j}}{\partial x_j} = -\bar{J}, \\
\frac{\partial 0.5\rho V_{1i}}{\partial t} + \frac{\partial 0.5(\rho V_{1j}V_{1i} + \delta_{ij}p - \sigma_{1ji})}{\partial x_j} = \bar{f}_i, \\
\frac{\partial 0.5\rho V_{2i}}{\partial t} + \frac{\partial 0.5(\rho V_{2j}V_{2i} + \delta_{ij}p - \sigma_{2ji})}{\partial x_j} = -\bar{f}_i.
\end{cases} \quad (4)$$

Let's transform system (4) into another form. The first equation is obtained by adding the first two equations in (4), and the second equation is obtained by subtracting them. We do the same with the third and fourth equations in (4). Taking into account the relationships $V_{1i} = \bar{V}_i + \vartheta_i, V_{2i} = \bar{V}_i - \vartheta_i$, we obtain the final system

$$\begin{cases} \frac{\partial \rho}{\partial t} + \frac{\partial \rho \overline{V_j}}{\partial x_j} = 0, \\ \frac{\partial \rho \vartheta_j}{\partial x_j} = 2\bar{J}, \\ \frac{\partial \rho \overline{V_i}}{\partial t} + \frac{\partial(\rho \overline{V_j} \overline{V_i} + \delta_{ji}\bar{p})}{\partial x_j} = \frac{\partial(\Pi_{ji} - \rho \vartheta_j \vartheta_i)}{\partial x_j}, \\ \frac{\partial \rho \vartheta_i}{\partial t} + \frac{\partial}{\partial x_j}(\rho \overline{V_j} \vartheta_i + \rho \vartheta_j \overline{V_i} - \pi_{ji}) = 2\bar{f}_i, \\ \Pi_{ji} = \mu\left(\frac{\partial \bar{V}_i}{\partial x_j} + \frac{\partial \bar{V}_j}{\partial x_i}\right), \pi_{ji} = \mu\left(\frac{\partial \vartheta_i}{\partial x_j} + \frac{\partial \vartheta_j}{\partial x_i}\right), \\ \qquad \bar{f}_i = \frac{1}{T}\int_{t-T/2}^{t+T/2}(f_i - \alpha_i p')d\tau. \end{cases} \tag{5}$$

System (6) represents the fundamental equations of Malikov's two-fluid approach to the mathematical description of turbulence. As can be seen from (5), the equation of motion for the averaged flow has a form very similar to the averaged Reynolds equation.

2.2 Auxiliary equations

The work (Malikov, 2020) describes in detail the methods for determining the interaction forces between liquids $\bar{f}_i$. Therefore, we present their final form here:

$$\begin{cases} 2\bar{f}_i = 2\bar{V}_i\bar{J} + \rho(F_{si} + F_{fi} + F_{mi}), \vec{F}_s = C_s rot\overline{\vec{V}} \times \vec{\vartheta}, \\ \vec{F}_i = -K_f\vec{\vartheta}, F_{mi} = 2\frac{\partial}{\partial x_j}\left[\nu_{ji}\left(\frac{\partial \vartheta_i}{\partial x_j} + \frac{\partial \vartheta_j}{\partial x_i}\right)\right], \\ \nu_{ji} = 3\nu + 2\left|\frac{\vartheta_i \vartheta_j}{def(\overline{V})}\right| npui \neq j, \nu_{ii} = 3\nu + \frac{1}{div\vec{\vartheta}}\left|\frac{\vartheta_k \vartheta_k}{def(\overline{V})}\right|\frac{\partial \vartheta_k}{\partial x_k}. \end{cases} \tag{6}$$

here $2\bar{V}_i\bar{J}$ – force caused by mass transfer between liquids; F_{si} – Saffman transverse force due to the shear velocity field; F_{fi} – frictional force; F_{mi} – the force resulting from the relative molar motion of liquids; $def(\overline{\vec{V}}) = \sqrt{2S_{ij}}S_{ij}, S_{ij} = \frac{1}{2}\left(\frac{\partial \bar{V}_i}{\partial x_j} + \frac{\partial \bar{V}_j}{\partial x_i}\right)$ – strain rate.

Substituting expressions (6) into system of equations (5), we obtain the following system of equations for turbulent incompressible flow in the two-fluid approach.

A symmetrical law of mass transfer between the fluids is introduced, ensuring conservation of momentum;

Turbulent viscosity is derived from first principles through the relative motion of the fluids, without the use of semi-empirical functions;

The model correctly describes anisotropic and separated flows, where linear RANS models give errors.

$$\begin{cases} \frac{\partial \overline{V_j}}{\partial x_j} = 0, \\ \frac{\partial \overline{V_i}}{\partial t} + \overline{V_j}\frac{\partial \overline{V_i}}{\partial x_j} + \frac{\partial \bar{p}}{\rho \partial x_i} = \frac{\partial}{\partial x_j}\left[\nu\left(\frac{\partial \bar{V}_i}{\partial x_j} + \frac{\partial \bar{V}_j}{\partial x_i}\right) - \vartheta_j\vartheta_i\right], \\ \frac{\partial \vartheta_i}{\partial t} + \overline{V_j}\frac{\partial \vartheta_i}{\partial x_j} = -\vartheta_j\frac{\partial \overline{V_i}}{\partial x_j} + \frac{\partial}{\partial x_j}\left[\nu_{ji}\left(\frac{\partial \vartheta_i}{\partial x_j} + \frac{\partial \vartheta_j}{\partial x_i}\right)\right] + F_{si} + F_{fi}, \\ \nu_{ji} = 3\nu + 2\left|\frac{\vartheta_i\vartheta_j}{def(\overline{\vec{V}})}\right| i \neq j, \nu_{ii} = 3\nu + \frac{1}{div\vec{\vartheta}}\left|\frac{\vartheta_k\vartheta_k}{def(\overline{\vec{V}})}\right|\frac{\partial \vartheta_k}{\partial x_k}, \\ \vec{F}_f = -K_f\vec{\vartheta}, \vec{F}_s = C_s rot\overline{\vec{V}} \times \vec{\vartheta}. \end{cases} \tag{7}$$

where K_f the coefficient of friction, is given by:

$$K_f = C_1\lambda 2\frac{|\vec{d}\cdot\vec{\vartheta}|}{d^2}{}_{max} \tag{8}$$

In this expression, d represents the minimum distance from the flow point under consideration to the nearest solid wall. This value is used to determine the friction coefficient and is calculated based on the local geometry of the computational grid. For an arbitrary geometric configuration, d is defined as the shortest distance from the field point under consideration to the solid wall. Fig. 2 schematically shows the principle for calculating the minimum distance.

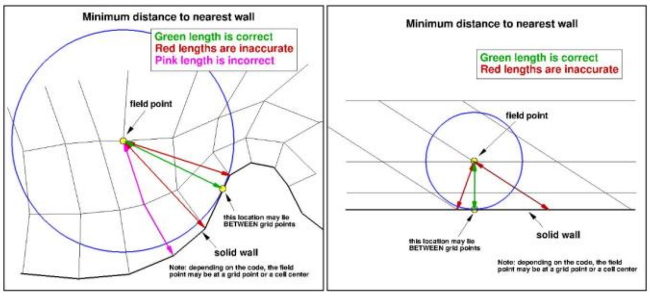

Fig. 2. Principle of calculating the minimum distance.

λ_{max} the largest root of the characteristic equation

$$det(A - \lambda E) = 0, \tag{9}$$

Where at $\vec{\zeta} = rot\overline{\vec{V}}$,

$$A = \begin{vmatrix} -\frac{\partial \bar{V}_1}{\partial x_1} - \frac{\partial \bar{V}_1}{\partial x_2} - C_s\zeta_3 - \frac{\partial \bar{V}_1}{\partial x_3} + C_s\zeta_2 \\ -\frac{\partial \bar{V}_2}{\partial x_1} + C_s\zeta_3 - \frac{\partial \bar{V}_2}{\partial x_2} - \frac{\partial \bar{V}_2}{\partial x_3} - C_s\zeta_1 \\ -\frac{\partial \bar{V}_3}{\partial x_1} - C_s\zeta_2 - \frac{\partial \bar{V}_3}{\partial x_2} + C_s\zeta_1 - \frac{\partial V_3}{\partial x_3} \end{vmatrix}. \tag{10}$$

Test problems show that adequate results are obtained when $C_1 = 0.7825; C_2 = 0.306; C_s = 0.2$. Malikov's model has been successfully tested in calculations of flow past plates, round and plane jets, diffusers, and multicomponent flows with variable density. Its advantage is its ability to physically justify turbulent stresses, adequately describe separated flows, and require much less computational resources than LES models with comparable accuracy.

2.3 Dimensionless form of equations

The system of equations is rendered, dimensionless by using characteristic length and velocity scales. All velocity components are normalized to the free-stream velocity U_0, and the coordinates are normalized to the side length of the square cylinder d. Thus:

$$U = \frac{\overline{V_1}}{U_0}, V = \frac{\overline{V_2}}{U_0}, \; u = \frac{\vartheta_1}{U_0}, \vartheta = \frac{\vartheta_2}{U_0}, \quad x = \frac{x_1}{d}, \quad y = \frac{x_2}{d}, \quad \tau = \frac{tU_0}{d}, \quad p^* = \frac{p}{\rho U_0^2}. \tag{11}$$

After introducing these dimensionless variables, equations (7) take the dimensionless form:

$$\begin{cases} \frac{\partial U}{\partial x}+\frac{\partial V}{\partial y}=0, \\ \frac{\partial U}{\partial t}+\frac{\partial UU}{\partial x}+\frac{\partial VU}{\partial y}+\frac{1}{\rho}\frac{\partial p}{\partial x}=-\frac{\partial uu}{\partial x}-\frac{\partial u\vartheta}{\partial y}+ \\ \qquad \frac{1}{Re\left(\frac{\partial^2 U}{\partial x^2}+\frac{\partial^2 U}{\partial y^2}\right)} \\ \frac{\partial V}{\partial t}+\frac{\partial UV}{\partial x}+\frac{\partial VV}{\partial y}+\frac{1}{\rho}\frac{\partial p}{\partial y}=-\frac{\partial u\vartheta}{\partial x}-\frac{\partial \vartheta\vartheta}{\partial y}+ \\ \qquad \frac{1}{Re\left(\frac{\partial^2 V}{\partial x^2}+\frac{\partial^2 V}{\partial y^2}\right)} \\ \frac{\partial u}{\partial t}+\frac{\partial Uu}{\partial x}+\frac{\partial Vu}{\partial y}=-u\frac{\partial U}{\partial x}-\vartheta\frac{\partial U}{\partial y}+ \\ \qquad C_s\vartheta\left(\frac{\partial U}{\partial y}-\frac{\partial V}{\partial x}\right)+\frac{\partial}{\partial x}\left(2\nu_{xx}\frac{\partial u}{\partial x}\right)+ \\ \qquad \frac{\partial}{\partial y}\left[\nu_{xy}\left(\frac{\partial u}{\partial y}+\frac{\partial \vartheta}{\partial x}\right)\right]-K_f u, \\ \frac{\partial \vartheta}{\partial t}+\frac{\partial U\vartheta}{\partial x}+\frac{\partial V\vartheta}{\partial y}=-u\frac{\partial V}{\partial x}-\vartheta\frac{\partial V}{\partial y}- \\ \qquad C_s u\left(\frac{\partial U}{\partial y}-\frac{\partial V}{\partial x}\right)+\frac{\partial}{\partial y}\left(2\nu_{yy}\frac{\partial \vartheta}{\partial y}\right)+ \\ \qquad \frac{\partial}{\partial x}\left[\nu_{xy}\left(\frac{\partial u}{\partial y}+\frac{\partial \vartheta}{\partial x}\right)\right]-K_f\vartheta.\{ \end{cases} \tag{12}$$

Here $Re=\frac{\rho U_0 d}{\mu}$ – Reynolds number.

$$\nu_{xy}=\frac{3}{Re}+\frac{|u\vartheta|}{\mathrm{def}\,(\vec{V})},\ \nu_{xx}=\nu_{yy}\frac{3}{Re}+\frac{S}{\mathrm{def}\,(\vec{V})},\ S=\frac{u^2+\vartheta^2 J_y}{J_x+J_y},\ J_x=\left|\frac{\partial u}{\partial x}\right|,\ J_y=\left|\frac{\partial \vartheta}{\partial y}\right|,\ \mathrm{def}(\vec{V})=\sqrt{2\left[\frac{\partial U}{\partial x}+\frac{\partial V}{\partial y}\right]^2+\left[\frac{\partial U}{\partial y}\right]^2+\left[\frac{\partial V}{\partial x}\right]^2} \tag{13}$$

In the above equations, U,V are the longitudinal and transverse components of the vector of average flow velocity, respectively, p is the static pressure, u,ϑ are the relative axial and transverse components of the fluid velocity, V is the molecular kinematic viscosity, ν_{xx}, ν_{yy}, ν_{xy}, are the effective molar viscosities, d is the nearest distance to the solid wall, λ_{max} is the largest root of the characteristic equations

$$det\begin{vmatrix}\lambda+\frac{\partial U}{\partial x}(1-C_s)\frac{\partial U}{\partial y}+C_s\frac{\partial V}{\partial x} \\ C_s\frac{\partial U}{\partial y}+(1-C_s)\frac{\partial V}{\partial x}\lambda+\frac{\partial V}{\partial y}\end{vmatrix}=0. \tag{14}$$

The largest root of this equation is

$$\lambda\sqrt{C_s(1-C_s)\left[\frac{\partial U}{\partial y}-\frac{\partial V}{\partial x}\right]^2+\frac{\partial U}{\partial y}\frac{\partial V}{\partial x}-\frac{\partial U}{\partial x}\frac{\partial V}{\partial y}}_{max} \tag{15}$$

Consequently, all calculation results presented in the work are given in dimensionless form: velocities are normalized to the inlet flow velocity, and distances are normalized to the length of the side of a square cylinder.

2.4 Solution domain and boundary conditions

Malikov's two-fluid turbulence model is applied to investigate the flow around one and two square cylinders located side by side at a Reynolds number of Re=47,000. The computational domain and boundary conditions are shown in Fig. 3 (a, b). The domain has a rectangular shape with dimensions of $10d\times 24d$, where d=1 is the side length of the square cylinder, taken as the characteristic dimension. The inlet velocity U_0 is used as the characteristic velocity for dimensionless transformation. The center of the cylinder is located at the origin (0,0).

The boundary conditions are specified as follows. At the inlet (left boundary): uniform velocity profile $U=U_0$, V=0, pressure p=0, and zero gradient in the y direction: $\partial u/\partial y$=0; At the outlet (right boundary): zero gradient conditions for all variables $\partial u/\partial x$=0, $\partial v/\partial x$=0, $\partial p/\partial x$=0; At the upper and lower boundaries: symmetry conditions $\partial u/\partial y$=0, $\partial v/\partial y$=0; On the cylinder surface: no-slip conditions $u=v$=0 fig. 3 (a, b).

For two adjacent cylinders, the distance between their centers, T/d, was varied, allowing us to study the influence of the intercylinder clearance on the interaction of vortex structures and the characteristics of wake formation. All outer boundaries of the computational domain were located at a sufficient distance from the bodies to eliminate the influence of blocking effects and ensure the correct development of the Karman vortex street.

In this study, no wall functions were used to calculate turbulent flow near solid walls. This is because Malikov's two-fluid model is a low-Reynolds-number turbulence model in which the equations are integrated down to the wall, including the viscous sublayer. This solution provides a more accurate description of the velocity distribution and turbulent viscosity in the near-wall region. It should be noted that Malikov's model (Malikov, 2020) was originally developed as a low-Reynolds-number turbulence model, designed for direct integration through the wall layer without the use of empirical wall functions. This allows for the inclusion of small-scale vortex structures and the accurate description of transient flow regimes near the wall.

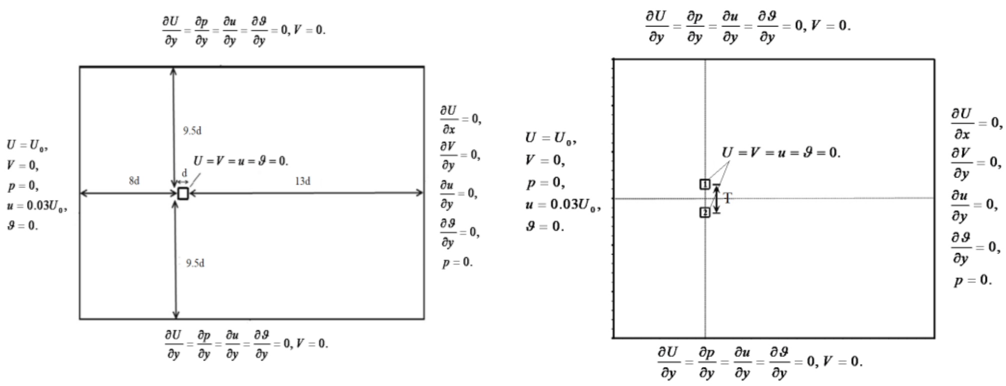

Fig. 3. Two-dimensional computational domain and boundary conditions for flow around one and two adjacent square cylinders.

2.5 The cases considered

To study the influence of the distance between the cylinders on the flow structure and the vortex wake characteristics, seven different cases corresponding to different interval ratios T/d were considered. The values of T/d were taken equal to 0, 1.02, 1.12, 1.75, 2.4, 3.5, and 5, which made it possible to trace the transition from the regime of close interaction of vortex streets to the regime of virtually independent flow past the cylinders. The calculations were performed at a fixed time step of Δt=0.001, which ensures the stability of the solution and sufficient temporal resolution to describe periodic vortex structures. The grid resolution details are given in Table 1. The node numbers are 40,000. For the case of T/d=0 and T/d=2.4.

Table 1. Mesh details in different cases for flow around one or two square cylinders located next to each other at Re=47000.

Model	Interval ratios T/d	Amount of elements	Δt
Malikov	0 1.02 1.12 1.75 2.4 3.5 5	40 000	0.001

3 NUMERICAL METHODS
3.1 Computational mesh and discretization

The system of equations (12) can be represented in matrix form:

$$\frac{\partial \Phi}{\partial t} + U\frac{\partial \Phi}{\partial x} + V\frac{\partial \Phi}{\partial y} = \frac{\partial}{\partial x}\left(A\frac{\partial \Phi}{\partial x}\right) + \frac{\partial}{\partial y}\left(B\frac{\partial \Phi}{\partial y}\right) + \Pi^{\Phi} \quad (16)$$

Here, (see equation 17).

A second-order upwind scheme was used to approximate the convective terms in the transport equations. Partial derivatives with respect to the x and y coordinates were approximated depending on the flow direction as follows:

$$\left(\frac{\partial \Phi}{\partial x}\right) = \begin{cases} \frac{3\Phi_{i,j}^{n} - 4\Phi_{i-1,j}^{n} + \Phi_{i-2,j}^{n}}{2\Delta x}, & U > 0, \\ \frac{-\Phi_{i+2,j}^{n} + 4\Phi_{i+1,j}^{n} - 3\Phi_{i,j}^{n}}{2\Delta x}, & U < 0, \end{cases} \left(\frac{\partial \Phi}{\partial y}\right) = \begin{cases} \frac{3\Phi_{i,j}^{n} - 4\Phi_{i,j-1}^{n} + \Phi_{i,j-2}^{n}}{2\Delta y}, & V > 0, \\ \frac{-\Phi_{i,j+2}^{n} + 4\Phi_{i,j+1}^{n} - 3\Phi_{i,j}^{n}}{2\Delta y}, & V < 0. \end{cases} \quad (18)$$

This scheme provides a more accurate representation of momentum and energy flows compared to the first order approximation and allows for the reduction of numerical diffusion distortions at large velocity gradients.

A mixed difference scheme was used to numerically solve the equations. The terms along the x axis were approximated explicitly, while those along the y axis were approximated implicitly. This approach provides a balance between computational stability and calculation speed, since explicit approximation along the x axis simplifies the calculations, while implicit approximation along the y axis improves the stability of the solution. An implicit second-order scheme was used to approximate the diffusion terms along the y coordinate, and the sweep method (Thomas's method) (Thomas, 1949)was used to solve the resulting tridiagonal system of linear algebraic equations. This allowed us to efficiently determine the unknown values of the Φ function at each time step while maintaining high accuracy and stability of the calculation.

$$\left(\frac{\partial \Phi}{\partial x}\right) = \frac{\Phi_{i+1,j}^{n} - 2\Phi_{i,j}^{n} + \Phi_{i-1,j}^{n}}{\Delta x}, \left(\frac{\partial \Phi}{\partial y}\right) = \frac{\Phi_{i,j+1}^{n+1} - 2\Phi_{i,j}^{n+1} + \Phi_{i,j-1}^{n+1}}{\Delta y} \quad (19)$$

The simulation was started at time t = 0 s and simulated up to t = 500 using a fixed Courant number of 1. The velocity field was calculated across the width and averaged over time over the period between 200 ≤ t ≤ 500 s.

Fig. 4(a, b) shows a diagram of a grid consisting of quadrangular elements for the flow region. In the case of two cylinders, the rectangular computational domain expands to 10dx24d (Fig. 4b). The centers of the two square cylinders, "1" and "2", are (0, ± T/2), so the ratio of the distance between the centers of the two cylinders can be defined as T/d, where d = 1 has the same definition as in case above.

$$\Phi = \begin{pmatrix} U \\ V \\ u \\ \vartheta \end{pmatrix}, A = \begin{pmatrix} \frac{1}{Re} \\ \frac{1}{Re} \\ 2v_{xx} \\ v_{xy} \end{pmatrix}, B = \begin{pmatrix} \frac{1}{Re} \\ \frac{1}{Re} \\ v_{xy} \\ 2v_{yy} \end{pmatrix}, \Pi^{\Phi} = \begin{pmatrix} -\frac{\partial p}{\rho \partial x} - \frac{\partial u\vartheta}{\partial y} - \frac{\partial uu}{\partial x} \\ -\frac{\partial p}{\rho \partial y} - \frac{\partial \vartheta\vartheta}{\partial y} - \frac{\partial u\vartheta}{\partial x} \\ -\left(u\frac{\partial U}{\partial x} + \vartheta\frac{\partial U}{\partial y}\right) + \frac{\partial}{\partial y}\left(v_{xy}\left(\frac{\partial \vartheta}{\partial x}\right)\right) + C_s\left(-\left(\frac{\partial V}{\partial x} - \frac{\partial U}{\partial y}\right)\vartheta\right) - K_f u \\ -\left(u\frac{\partial V}{\partial x} + \vartheta\frac{\partial V}{\partial y}\right) + \frac{\partial}{\partial x}\left(v_{xy}\left(\frac{\partial u}{\partial y}\right)\right) + C_s\left(\left(\frac{\partial V}{\partial x} - \frac{\partial U}{\partial y}\right)u\right) - K_f \vartheta \end{pmatrix}. \quad (17)$$

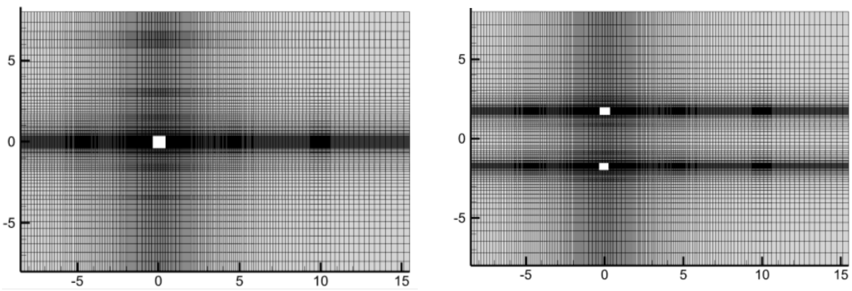

Fig. 4. Two-dimensional grid consisting of quadrangular elements for the flow region.

The computational code is executed using the 64-bit Intel platform. All calculations were performed on a computer with an Intel i5-7800HQ quad-core processor, 2.5 GHz, 16 GB DDR3 memory, 512 GB hard disk, and Windows 7 (64-bit) operating system.

3.2 Solution procedure

Correction of velocity through pressure was carried out using the SIMPLE method (Patankar, 2018; Patankar & Spalding, 1972).

$$\begin{cases} \overline{U}^{n+1} = U^{n+1} - \Delta t \frac{\partial \delta p}{\partial x}, \\ \overline{V}^{n+1} = V^{n+1} - \Delta t \frac{\partial \delta p}{\partial y}. \end{cases} \tag{20}$$

It should be noted that all governing equations are expressed in dimensionless form. The density is normalized by the reference (free-stream) density $\rho_0 = 1.0$, which leads to its implicit inclusion in the non-dimensional variables. Therefore, the density term does not explicitly appear in Eq. (20). Equation (20) U^{n+1}, V^{n+1} denotes the intermediate grid function for the velocity vector; $\delta p = p^{n+1} - p^n$ is the pressure correction. Multiplying equation (20) by the gradient and taking into account the solenoidality of the velocity vector at the (n+1)-th time layer, we obtain the Poisson equation for determining the pressure correction:

$$\Delta t \left(\frac{\partial^2 \delta p}{\partial x^2} + \frac{\partial^2 \delta p}{\partial y^2} \right) = \frac{\partial V^{n+1}}{\partial x} + \frac{\partial V^{n+1}}{\partial y}. \tag{21}$$

The solution of a stationary problem is carried out using the method of establishing time, therefore dependence (21) is written in the form of a non-stationary differential equation

$$\frac{\partial \delta p}{\partial t_0} - \Delta t \left(\frac{\partial^2 \delta p}{\partial x^2} + \frac{\partial^2 \delta p}{\partial y^2} \right) = \frac{\partial V^{n+1}}{\partial x} + \frac{\partial V^{n+1}}{\partial y}. \tag{22}$$

where the fictitious time t0 is an iteration parameter. When solving equation (22), for the time step, we can write $\Delta t_0 = a_1 \Delta t$, with the value of the constant a_1 typically being less than one and chosen to ensure rapid convergence of the numerical process.

The equation for the pressure correction in system (22) has an elliptical form. Calculating the pressure equation (22) using the alternating direction method requires significant time. In our case, the Gauss-Seidel method (Ferziger and Perić, 2002) was used to solve the equations. This allowed us to limit the calculation to a single-direction run, which somewhat reduced the computational costs while still ensuring sufficient accuracy for our purposes.

$$\frac{\delta p_{i,j}^{n+1} - \delta p_{i,j}^{n}}{\Delta t_0} - \left(\frac{\delta p_{i+1,j}^{n} - 2\delta p_{i,j}^{n+1} + \delta p_{i-1,j}^{n}}{\Delta x^2} \right) - \left(\frac{\delta p_{i,j+1}^{n+1} - 2\delta p_{i,j}^{n+1} + \delta p_{i,j-1}^{n+1}}{\Delta y^2} \right) = \frac{1}{\Delta t} \left(\frac{U_{i,j}^{n+1} - U_{i-1,j}^{n+1}}{\Delta x} + \frac{V_{i,j}^{n+1} - V_{i,j-1}^{n+1}}{\Delta y} \right) \tag{23}$$

Thus, from the system (18–19) the intermediate values of the parameters are determined, then the correction pressure is determined using equation (23) and in accordance with (20) the velocity vector on the (n+1) time layer and the pressure are determined, with $p^{n+1} = p^n + \delta p$. The Courant numbers for the computational grid were $Co_x = 0.0625, Co_y = 0.1876$.

4 RESULTS AND DISCUSSION

4.1 Vortex formation and wake vortex structure

This section presents numerical results of flow models in terms of vorticity distribution and averaged velocity fields. The instantaneous vorticity distributions obtained using the Malikov model at various distances are shown in Figs. 5 (a)–(g) as well as Fig. 5 shows the experimental results(Alam et al., 2011). It is found that the vorticity results are strongly affected by the distance between them. Three types of wake are observed in Fig. 5. a pattern with a single streamlined body (mode A), a slot flow interference pattern (mode B), and a synchronized pattern in antiphase (mode C).

On Fig. 5(a–c) shows a body structure with a single break (mode A), which typically occurs at one square or less distance ratio, eg T/d<1.3. This model is similar to a single cylinder with two long vortex streets behind (one positive and one negative), known as the Karman vortex street. This is because a smaller gap ratio results in much weaker flows in the gap between the two square cylinders. They are too weak to affect the wake flow, so the two cylinders behave like one streamlined body. A vortex pair is formed and periodically flies off the top side of cylinder 1 and the bottom side of cylinder 2.

At T/d = 1.3–2.2, the flow in the gap between the cylinders shifts with sufficient force, forming one narrow and one wide street (Fig. 5d), which are associated with high and low Strouhal number, respectively, and therefore are called slot flow (mode B).

On Fig. 5(e), where the separation ratio reaches T/d = 2.2–3.0, the patterns of the interference trace of the slot flow are presented. In this scheme, the distance between the cylinders increases, which increases the energy of the flow in the gap generated in the area between the two cylinders. The slit flow is strong enough to break away from the cylinders, interact with the vortices on the top side of cylinder 1 and the bottom side of cylinder 2, and regenerate an irregular and very complex wake flow (mode B).

Beyond T/d = 3.0, vortex formation from one cylinder is constantly associated with vortex formation from the other with the same frequencies, which is called the antiphase mode or (mode C) (Fig. 5f–g). In both of these examples, the distance between the cylinders is large enough for a vortex to form and descend down the top and bottom sides of each cylinder. Two symmetrical vortex lanes can be observed out of phase and synchronously, and each lane is formed by a pair of positive and negative vortices.

4.2 Longitudinal speeds

Figures. 6(a)–(g) show the time-averaged longitudinal velocity fields for various interval ratios.

Near wake characteristics in each flow regime, including wake width, vortex shedding length, recirculation bubble, and velocity recovery, can be explored by examining iso contours of the time-averaged longitudinal flow velocity. Fig. 6 shows the longitudinal velocity U in different modes, and also presents the experimental results. The same loop level increment is used to facilitate comparison.

Note the recirculation bubble is large for mode A (Fig. 6a–c) where the two cylinders act as a unit, resulting in a large effective cylinder width. The same is true for mode B behind the upper cylinder, i.e., on a wide street (Fig. 6d). On the contrary, this bubble is much smaller for the narrow street of mode B and mode C (Fig. 6e–g); as is the single-cylinder track. Accordingly, U quickly recovers in these modes, reaching 0.7 in the experiment and 0.65 in the numerical results at x/d=3–5. On the other hand, when the track consists of two streets of different widths, both of them show slower recovery than a single-cylinder track, although a narrow (lower) track is associated with a faster speed recovery than a wide one (Fig. 6d, e).

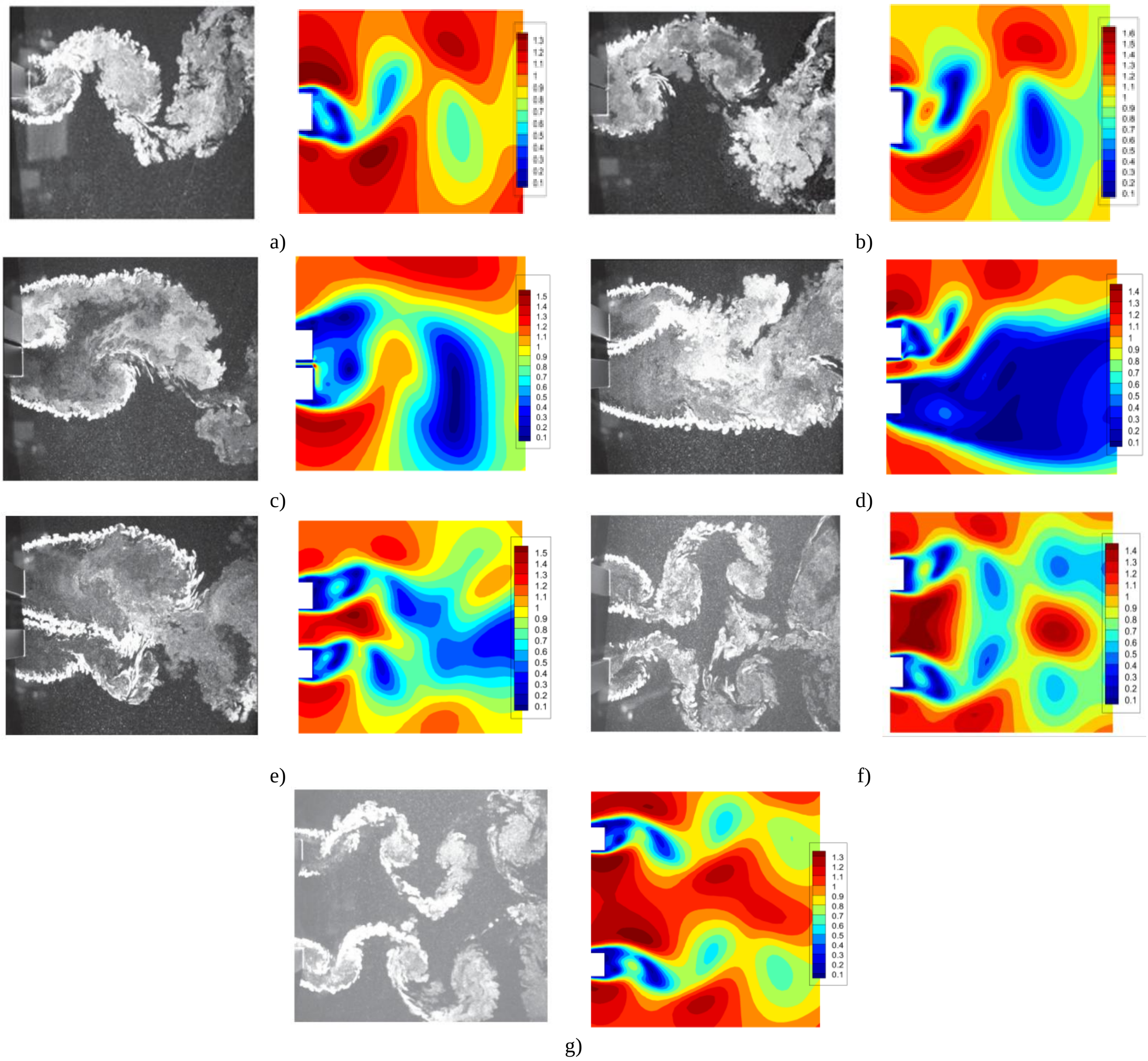

Fig. 5. Instantaneous vorticity distributions of the flow around one or two square cylinders with different distances T/d at Re=47000 study results (a-g-right) in comparison with the cited experimental work (a-g-left) at Re = 47000 according to (Alam et al., 2011), (a) T/d = 0, (b) T/d=1.02, (c) T/d=1.12, (d) T/d=1.75, (e) T/d=2.4, (f) T/d=3.5, (g) T/d=5.

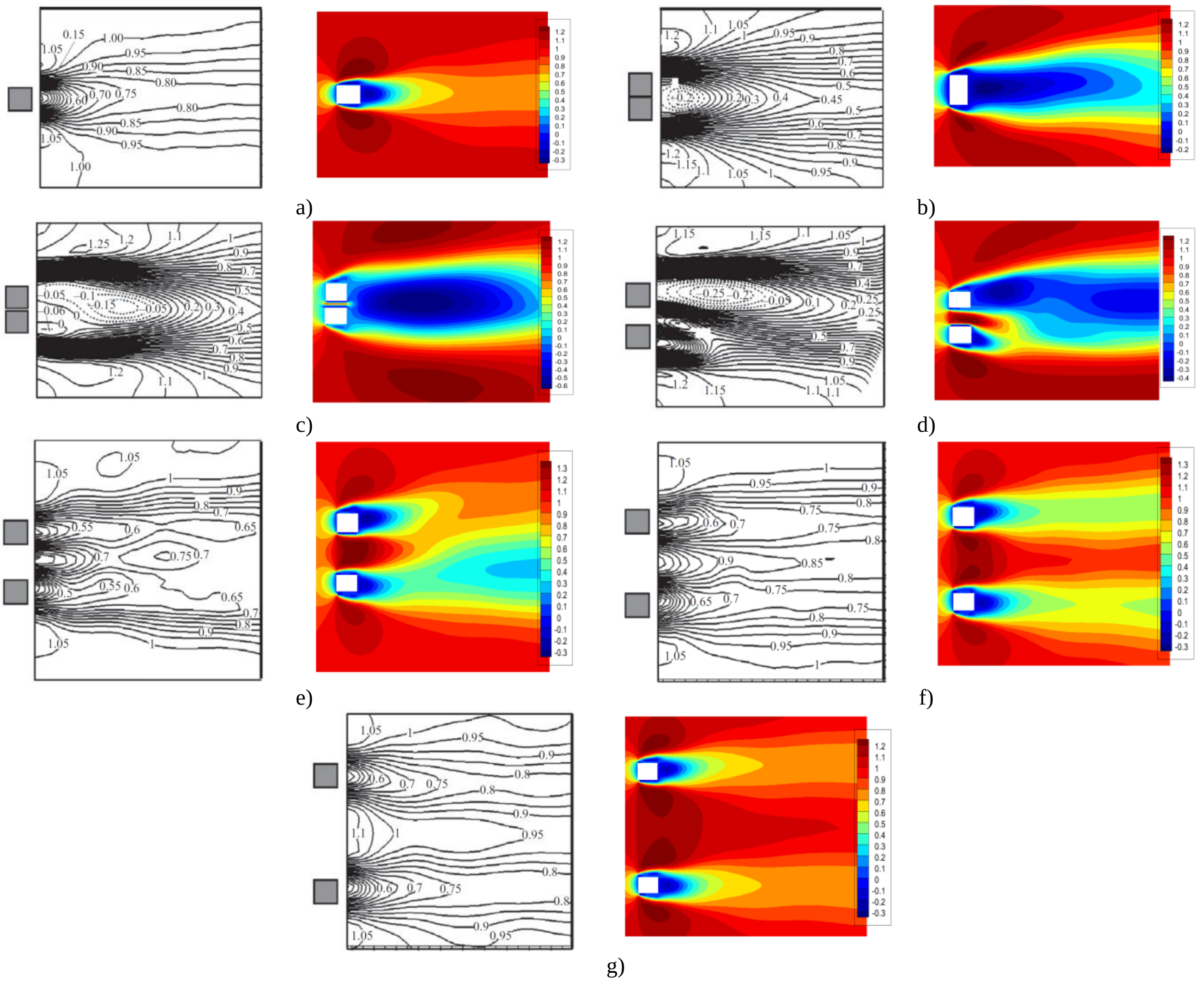

Fig. 6. Isocontours of the averaged longitudinal velocity U in flows around one or two square cylinders with different distances T/d at Re=47000 study results (a-g-right) in comparison with the cited experimental work (a-g-left) at Re = 47000 (Alam et al., 2011), (a) T/ d = 0, (b) T/d=1.02, (c) T/d=1.12, (d) T/d=1.75, (e) T/d=2.4, (f) T/d=3.5, (g) T/d=5.

4.3 Transverse velocities

Figs. 7(a)–(g) show the time-averaged lateral velocity fields for various interval ratios. An idea of the entrainment of the surrounding fluid in the wake, as well as the formation of vortices and the forces acting on the cylinders, can be obtained by examining the transverse velocity V in various modes (Fig. 7). In the wake behind a single isolated cylinder (Fig. 7a–c), positive and negative V as well as positive and negative V can be seen in modes B and C (Fig. 7d–g).

4.4 Longitudinal velocity profiles on the centerline

Fig. 8 shows the time-averaged longitudinal velocity on the central line of the channel for various interval ratios T/d = 0 to 5 and Re = 47000. The averaged velocity was compared with the experimental results (Alam et al., 2011).

4.5 Comparison of the speeds on the center lines of the first and second cylinders

Fig. 9 shows the time-averaged longitudinal velocities on the center line of the first and second cylinders for various interval ratios.

4.6 Cross-sectional velocity profiles x/d = 4

Fig. 10 shows the time-averaged longitudinal velocity per cross section x/d=4 for various interval ratios.

4.7 Time-averaged transverse velocities

Fig. 11 shows the time-averaged lateral velocity on the x/d=1 and x/d=2 sections for different interval ratios.

Fig.8–11 show thats the Malikov model very well describes the time-averaged velocity for the interval ratio T/d = 0–1.02 and 3.5-5. This is in mode A, T/d ≤ 1.02 where the two cylinders act as one. In mode C T/d ≥3.0 vortex formation from one cylinder is constantly associated with vortex formation from another with the same frequencies. In both of these examples, the distance between the cylinders is large enough for a vortex to form and travel down the top and bottom sides of each cylinder. In modes B. 1.02 < T/d < 3.5, the flow in the gap between the cylinders, forms one narrow and one wide street, which leads to flow instability.

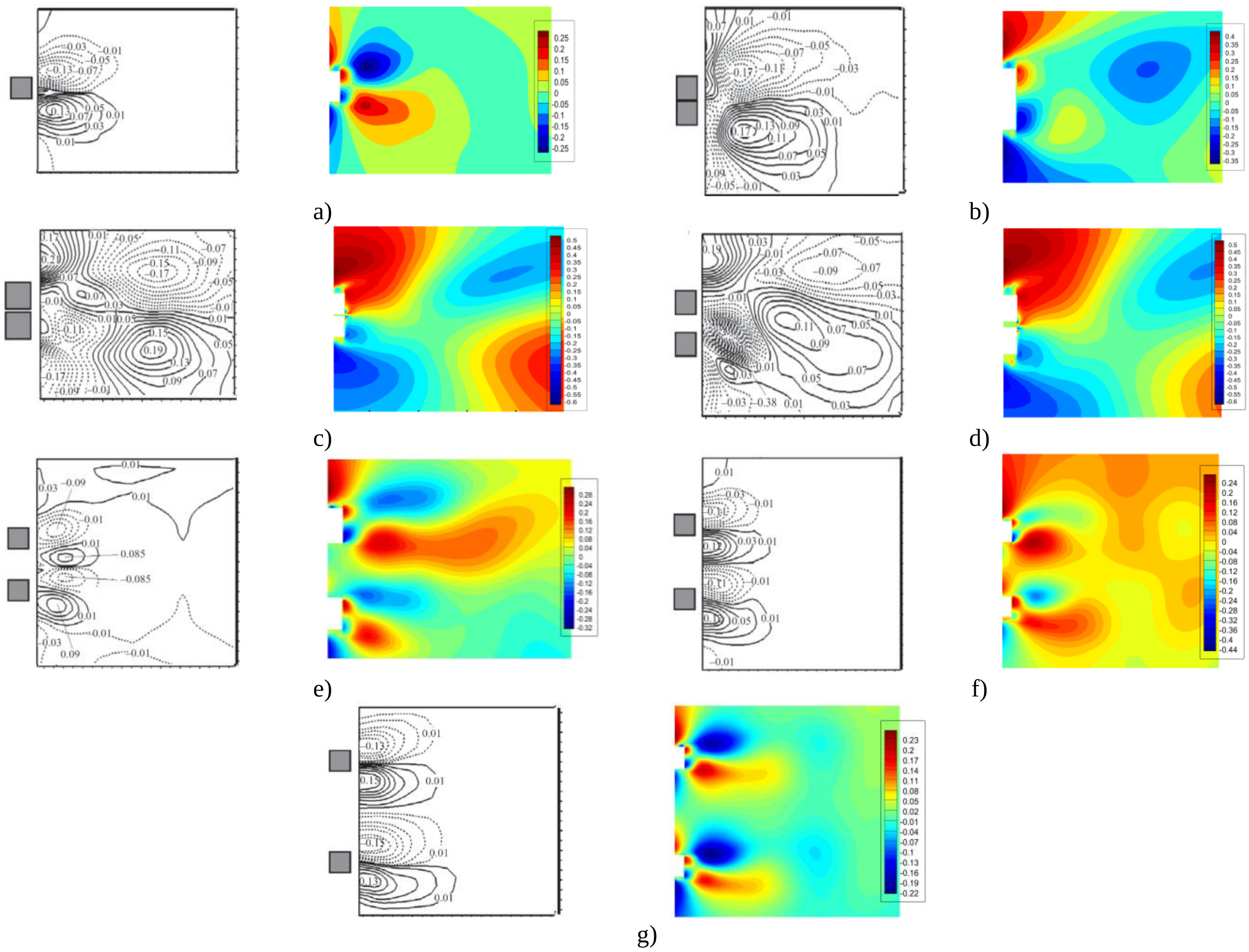

Fig. 7. Isocontours of the average transverse velocity V in the flows around one or two square cylinders with different distances T/d at Re=47000 study results (a-g-right) in comparison with the cited experimental work (a-g-left) at Re = 47000 (Alam et al., 2011), (a) T /d = 0, (b) T/d=1.02, (c) T/d=1.12, (d) T/d=1.75, (e) T/d=2.4, (f) T/d=3.5, (g) T/d=5.

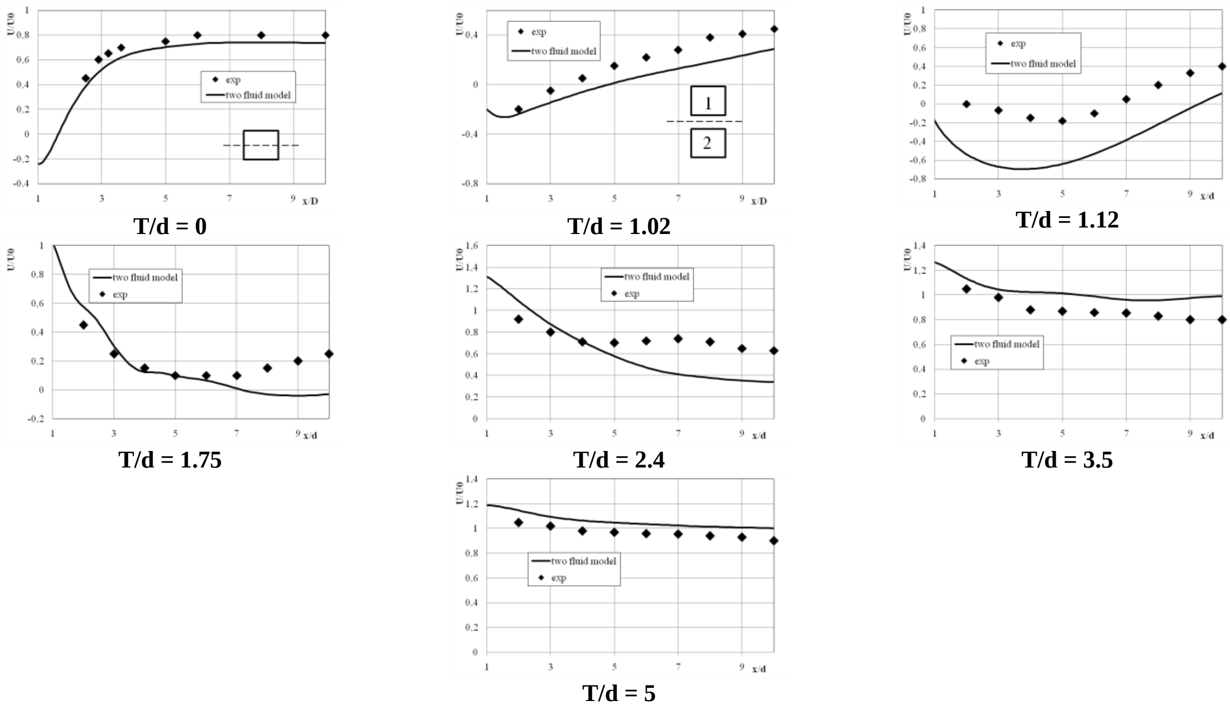

Fig.8. Time-averaged longitudinal velocity on the center line for different interval ratios.

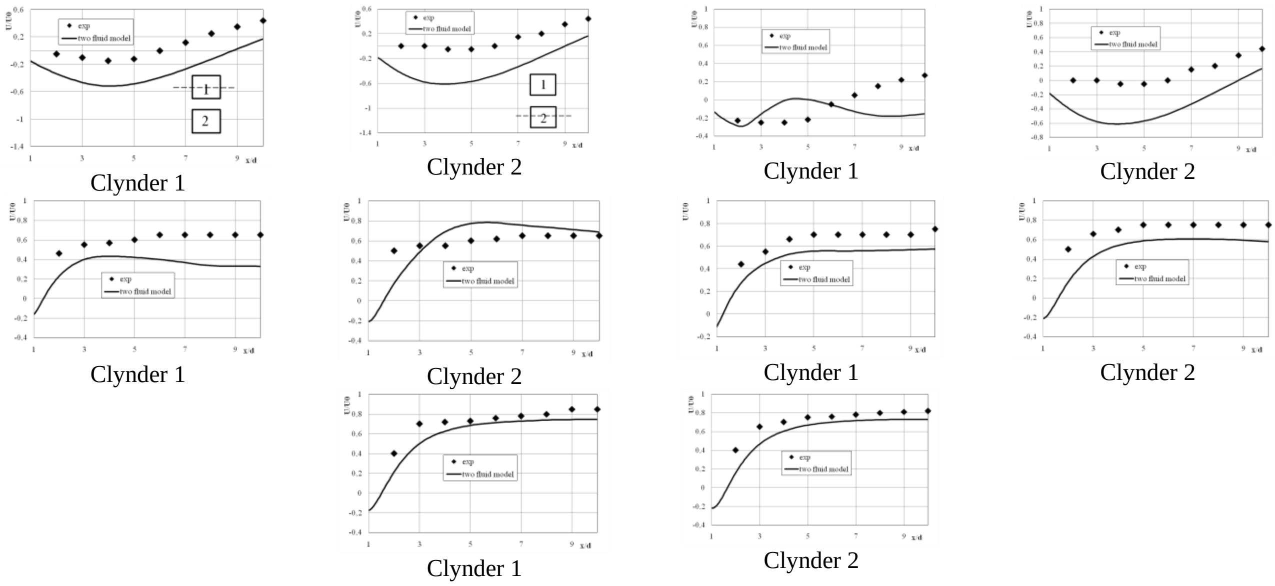

Fig. 9. Time-averaged longitudinal velocity on the center line of the first and second cylinders for different interval ratios.

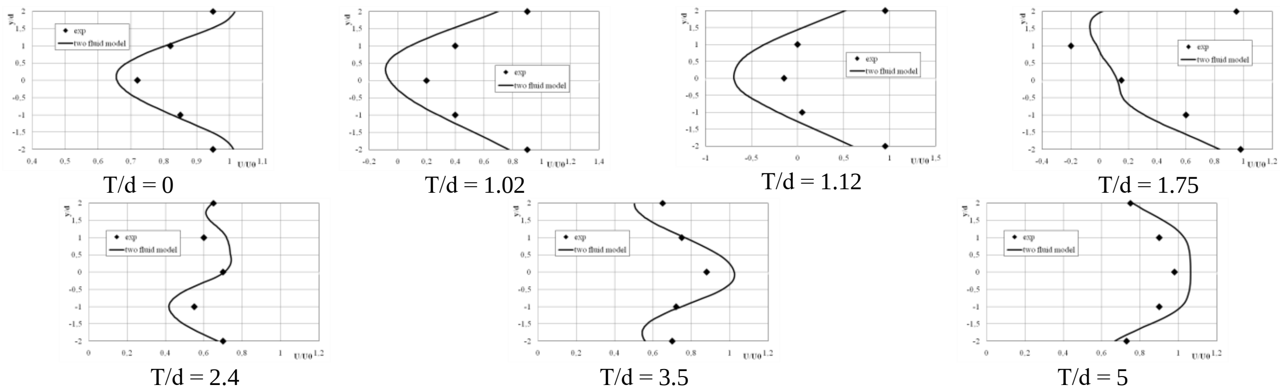

Fig. 10. Time-averaged longitudinal velocity per section x/d=4 for different interval ratios.

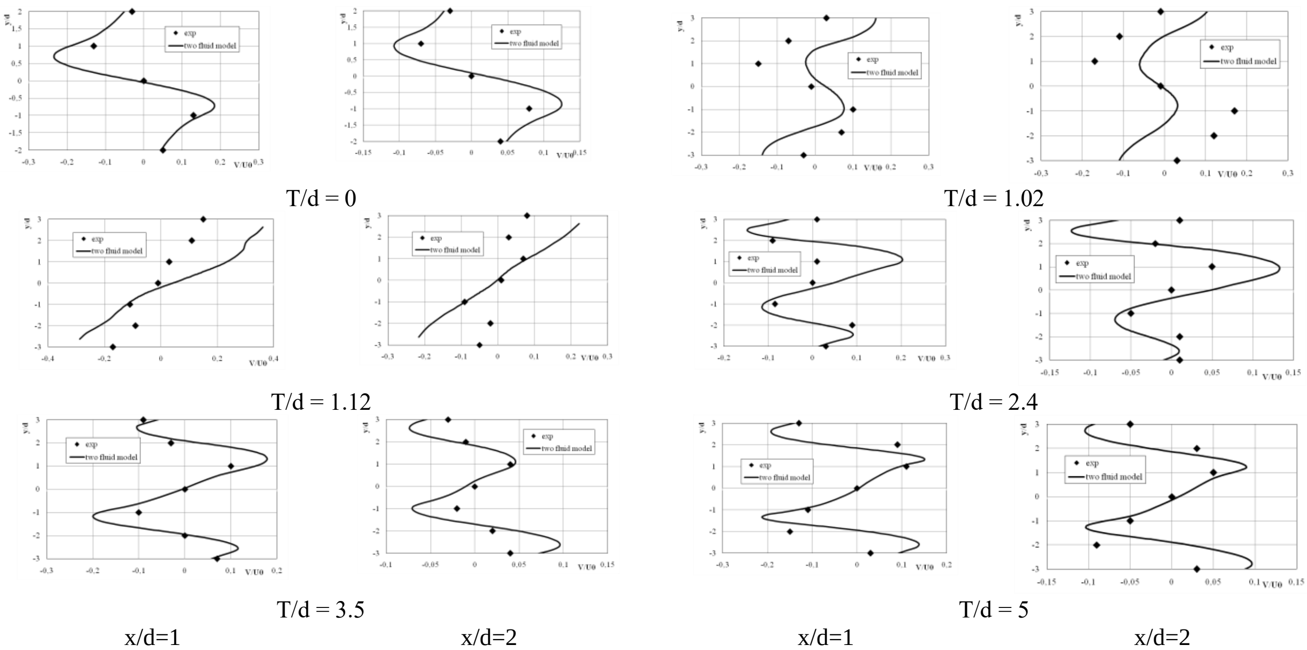

Fig. 11. Time-averaged lateral velocity for different interval ratios.

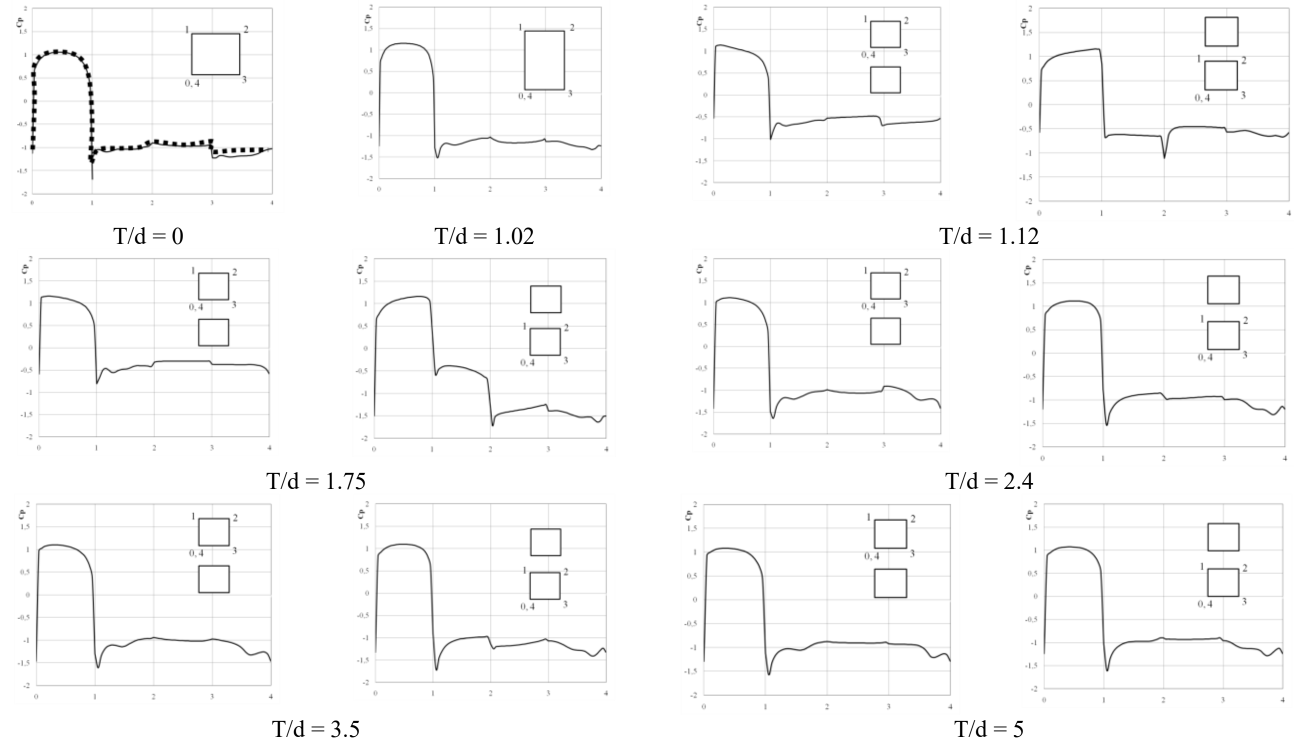

T/d = 0 T/d = 1.02 T/d = 1.12

T/d = 1.75 T/d = 2.4

T/d = 3.5 T/d = 5

Fig. 12. Surface pressure coefficients (Cp) along each face of a square cylinder.

4.8 Surface pressure coefficients

Fig. 12 shows the curves of the surface pressure coefficient (Cp) along each face at Re = 47000. The definition of C_p is: $C_p = \Delta p/(\rho U_0^2)$, where Δp is the static pressure drop across the surface of a square cylinder; ρ is the air density. Fig. 12 shows the Cp profile on a single square cylinder T/d = 0 and also shows the experimental data (black square). On the 0–1 face, Cp is symmetrical with respect to the critical point, where Cp reaches its maximum of 1.0. The minimum of Cp is 0.70 at vertices 0 and 1. On faces 1–2, Cp decreases from 1.2 (at vertex 1) to 0.9 (at vertex 2). On face 2–3, the point Cp is symmetric with respect to the center of face 2–3. The Cp curves on faces 1–2 and 3–4 were similar to each other due to geometric symmetry. From fig. Fig. 12 shows the Malikov two-fluid model (solid line) very well describes the surface pressure distribution of one cylindrical square.

Moreover, Fig. 12 shows Cp curves for two adjacent square cylinders, and for different spacing ratios. Fig. 12 display the Cp profile in the interval ratio T/d = 1.02. The distribution of Cp on faces 1–2 is similar to the distribution for a one-square cylinder T/d = 0. The profile of Cp on faces 1–2 is similar to the profile on faces 3–4 for a cylinder with one square. Fig. 12 also shows the distribution of Cp for various interval ratios from T/d = 1.02 to T/d = 5.

4.9 Time dependences of velocities and pressures

It is known that the so-called Karman path appears behind streamlined bodies, which has a periodic character. Therefore, the time behavior of the velocities behind the cylinders is of particular interest. Therefore, Fig. 13 shows the time dependences of the transverse velocities and pressures at x/d = 2 and y/d = 0.0.

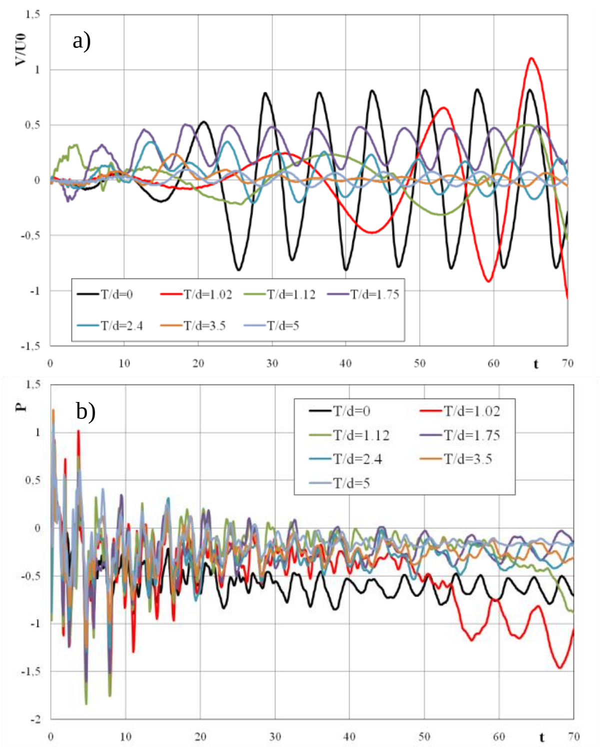

Fig. 13. Time dependences of a) transverse velocities and b) flow pressures at x/d = 2.0 and y/d = 0.0.

4.10 Vortex shedding frequencies and aerodynamic coefficients

To quantitatively evaluate the dynamic characteristics of the flow, the vortex shedding frequencies were calculated, expressed through the Strouhal number $St=fd/U_0$, where f is the pressure or velocity oscillation frequency, d is the characteristic size (the side of the square), and U_0 is the inlet flow velocity. The frequencies were determined based on the spectral analysis of the time dependences of the transverse velocity and pressure, presented in Fig. 13. The results showed that at $T/d \leq 1.2$, synchronous vortex formation is observed with a dominant frequency corresponding to $St \approx 0.13$–0.14, which is in good agreement with the experimental data (Alam et al., 2011). As the distance between the cylinders increases (T/d=2.4–3.5), the flow regime switches to antisynchronous (mode C), and the Strouhal number increases to $St \approx 0.15$–0.16, which is associated with the formation of independent vortex tracks behind each cylinder.

In addition, the coefficients of aerodynamic forces were calculated: drag C_d and lift C_l, determined by the expressions:

$$C_d = \frac{F_d}{\frac{1}{2}\rho U_0^2 d}, \qquad C_l = \frac{F_l}{\frac{1}{2}\rho U_0^2 d}. \tag{24}$$

where F_d and F_l are the projections of the integral pressure force and viscous friction on the x- and y-axes, respectively. The average values of C_d for a single cylinder were around 2.05, which is consistent with experimental data (Alam et al., 2011) and numerical results (Yen & Liu, 2011). For two-cylinder configurations at T/d=1.12–1.75, a slight decrease in C_d is observed due to flow shielding in the internal gap. At T/d>3.0, the values of C_d and C_l tend to the levels of a single cylinder, indicating weakening of the flow interaction. Thus, the calculated parameters (Strouhal number, drag and lift coefficients) demonstrate good agreement with experimental observations and confirm the correctness of the proposed two-fluid Malikov model in describing non-stationary flow characteristics.

4.11 Comparison of the two-fluid model with other turbulence models

To evaluate the accuracy of Malikov's two-fluid model, its results were compared with those of the widely used RANS (SST) and LES turbulence models. Calculations for the RANS and LES models were performed in ANSYS Fluent. In both cases, a three-dimensional geometry with a computational mesh containing approximately 2.5 million elements was used. In the LES approach, calculations were performed with a time step of $\Delta t = 1.5 \times 10^{-5}$, using the SIMPLE algorithm, and all equations were solved using second-order approximation (Second-Order Upwind). GPU accelerators were used to accelerate the calculations. In the RANS+SST model, the time step was $\Delta t = 5 \times 10^{-5}$, and calculations were performed on a CPU, also using second-order accurate schemes.

Fig. 14 compares the distributions of the dimensionless velocity behind a single square cylinder at Re=47000. Fig. 14a shows the distribution of the longitudinal velocity U/U_0 along the central axis of the wake, and Fig. 14b shows the velocity profile in the cross section x/d=4.

The figures show that the results of the two-fluid model (black curve) are in good agreement with experimental data (Alam et al., 2011). The LES model (blue curve) demonstrates comparable accuracy but requires significantly more computational resources. In turn, the RANS+SST model (red curve) underestimates the flow recovery rate in the recirculation zone.

The two-fluid code developed by the authors was executed in single-processor mode. The computation time for one typical case (Re = 47,000, single square cylinder) was approximately 9 hours. For comparison, a calculation using the RANS model (SST k–ω) in ANSYS Fluent on three processors took approximately 13 hours, and the LES model (2.5 million cells, $\Delta t = 1.5 \times 10^{-5}$) was executed on a GPU in 45 hours. Thus, the proposed two-fluid model provides comparable accuracy at significantly lower computational costs compared to the LES model.

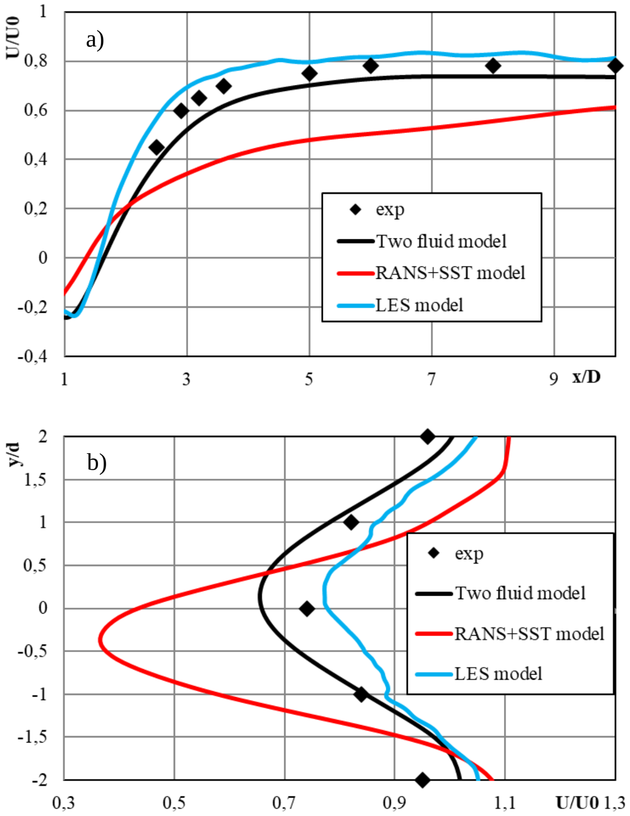

Fig.14. Dimensionless velocity distributions behind a single square cylinder.

5 CONCLUSIONS

This paper, demonstrated the capabilities of the recently developed Malikov two-fluid turbulence model, which is an improved version of the Spalding model. The model was applied to calculate turbulent flows past one and two square cylinders at the Reynolds number Re = 47,000. Seven cases of mutual distance between the cylinders T/d = 0, 1.02, 1.12, 1.75, 2.4, 3.5, and 5 were considered. The calculations showed that for a single cylinder, as well as for two cylinders at T/d ≤ 1.12 and T/d ≥ 3.5, the Malikov two-fluid model correctly reproduces the distribution of the mean pressure coefficient, the longitudinal velocity profiles, and the characteristic structures of the vortex wake. At intermediate distances (mode B, T/d ≈ 1.75–2.4), a slit flow regime with strong interference is observed, requiring further analysis and model refinement. The three resulting wake types, single, slit, and out-of-phase synchronous, are in good agreement with the experimental data. Comparison with the RANS (k–ω) and LES models, both implemented in ANSYS Fluent, showed that the proposed model provides results of similar accuracy with significantly lower computational costs. Thus, under identical conditions, the Malikov model calculation took approximately 9 hours of CPU time (1 processor), while RANS required 13 hours (3 processors), and LES required approximately 45 hours on the GPU. It should be noted that the calculations were performed in a two-dimensional setting to reduce the computational load. Further research will focus on applying the model to three-dimensional problems and more complex geometric configurations. The results obtained in this study confirm that the Malikov two-fluid model is a promising and computationally efficient tool for modeling turbulent flows in engineering applications.

Notations:

V_i = component of the average flow velocity
ϑ_i = component of the relative velocity
ν_{ji} = effective kinematic viscosity tensor arising from the relative motion of fluids
p = pressure in fluid mixture
K_f = scalar function of the friction force
C_s = shear coefficient
ν = molecular viscosity
t = time
C_1 = first constant in the coefficient of friction
C_2 = second constant in the coefficient of friction
λ_{max} = largest root of the characteristic equation
S_{ij} = strain rate tensor of a mixture of fluids
Re = Reynolds number
D = square height
d = nearest distance from a given point to a solid wall
ρ = density
RANS = Reynolds-averaged Navier–Stokes
SST = Shear Stress Transport
LES = Large Eddy Simulation
DNS = Direct numerical simulation

REFERENCES

Afgan, I., Kahil, Y., Benhamadouche, S., Sagaut, P., 2011. Large eddy simulation of the flow around single and two side-by-side cylinders at subcritical Reynolds numbers. Physics of Fluids, 23(7).

Alam, M.M., Zhou, Y., Wang, X.W., 2011. The wake of two side-by-side square cylinders. Journal of Fluid Mechanics, 669, 432–471.

Andrews, M.J., 1986. Turbulent mixing by Rayleigh-Taylor instability. Ph. D. Thesis, Imperial College, London.

Bao, Y., Zhou, D., Huang, C., Wu, Q., Chen, X., 2011. Numerical prediction of aerodynamic characteristics of prismatic cylinder by finite element method with Spalart–Allmaras turbulence model. Computers and Structures, 89(3–4), 325–338.

Ferziger, J. H., Perić, M., 2002. Computational methods for fluid dynamics (Vol. 586). Springer.

Fueyo, N., Malin, M.R., 2020. Brian Spalding and Turbulent Combustion. In: Runchal, A. (Ed.), 50 Years of CFD in Engineering Sciences. Springer, Singapore. https://doi.org/10.1007/978-981-15-2670-1_12

Haque, M.N., Katsuchi, H., Yamada, H., Nishio, M., 2013. Numerical simulation for effects of wind turbulence on flow field around rectangular cylinder. Journal of Structural Engineering A, 59, 605–615.

Huang, S., Li, Q.S., 2010. A new dynamic one-equation subgrid-scale model for large eddy simulations. International Journal for Numerical Methods in Engineering, 81(7), 835–865.

Inoue, O., Iwakami, W., Hatakeyama, N., 2006. Aeolian tones radiated from flow past two square cylinders in a side-by-side arrangement. Physics of Fluids, 18(4).

Kolář, V., Lyn, D. A., Rodi, W., 1997. Ensemble-averaged measurements in the turbulent near wake of two side-by-side square cylinders. Journal of Fluid Mechanics, 346, 201–237.

Li, A., Ahmadi, G., 1992. Dispersion and deposition of spherical particles from point sources in a turbulent channel flow. Aerosol Science and Technology, 16(4), 209–226.

Lim, H.C., Thomas, T.G., Castro, I.P., 2009. Flow around a cube in a turbulent boundary layer: LES and experiment. Journal of Wind Engineering and Industrial Aerodynamics, 97(2), 96–109.

Liu, D., Wu, C., Linden, K., Ducoste, J., 2007. Numerical simulation of UV disinfection reactors: Evaluation of alternative turbulence models. Applied Mathematical Modelling, 31(9), 1753–1769.

Madaliev, M., Mamadaliev, K., Hamdamov, M., 2025. Fluid dynamics simulation of twin square cylinders interaction using a two fluid turbulence model Malikov. AIP Conference Proceedings, 3265(1), 060014.

Malikov, Z.M., 2020. Mathematical model of turbulence based on the dynamics of two fluids. Applied Mathematical Modelling, 82, 409–436.

Malikov, Z.M., 2021. Mathematical model of turbulent heat transfer based on the dynamics of two fluids. Applied Mathematical Modelling, 91, 186–213.

Malikov, Z.M., 2022. Modeling a turbulent multicomponent fluid with variable density using a two-fluid approach. Applied Mathematical Modelling, 104, 34–49.

Malikov, Z.M., Madaliev, M.E., 2020. Numerical Simulation of Two-Phase Flow in a Centrifugal Separator. Fluid Dynamics, 55(8), 1012–1028.

Malikov, Z.M., Madaliev, M.E., 2022. Numerical simulation of separated flow past a square cylinder based on a two-fluid turbulence model. Journal of Wind Engineering and Industrial Aerodynamics, 231, 105171.

Malikov, Z.M., Madaliev, M.E., Chernyshev, S.L., Ionov, A.A., 2024. Validation of a two-fluid turbulence model in COMSOL multiphysics for the problem of flow around aerodynamic profiles. Scientific Reports, 14(1), 2306.

Markatos, N.C., Kotsifaki, C.A., 1994. One-dimensional, two-fluid modelling of turbulent premixed flames. Applied Mathematical Modelling, 18(12), 646–657.

Nozawa, K., Tamura, T., 2002. Large eddy simulation of the flow around a low-rise building immersed in a rough-wall turbulent boundary layer. Journal of Wind Engineering and Industrial Aerodynamics, 90(10), 1151–1162.

Patankar, S., 2018. Numerical heat transfer and fluid flow. CRC press.

Patankar, S.V., Spalding, D.B., 1972. A calculation procedure for heat, mass and momentum transfer in three-dimensional parabolic flows. In Numerical prediction of flow, heat transfer, turbulence and combustion (pp. 54–73). Elsevier.

Raissi, H., Shishesaz, M., Moradi, S., 2017. Applications of higher order shear deformation theories on stress distribution in a five layer sandwich plate. Journal of Computational Applied Mechanics, 48(2), 233–252.

Rusdin, A., 2017. Computation of turbulent flow around a square block with standard and modified k-ε turbulence models. International Journal of Automotive and Mechanical Engineering, 14(1), 3938–3953.

Shen, Y.M., Ng, C.-O., Chwang, A.T., 2003. A two-fluid model of turbulent two-phase flow for simulating turbulent stratified flows. Ocean Engineering, 30(2), 153–161.

Shimada, K., Ishihara, T., 2002. Application of a modified k–ε model to the prediction of aerodynamic characteristics of

rectangular cross-section cylinders. Journal of Fluids and Structures, 16(4), 465–485.
Sohankar, A., Davidson, L., Norberg, C., 2000. Large eddy simulation of flow past a square cylinder: comparison of different subgrid scale models. J. Fluids Eng., 122(1), 39–47.
Spalart, P., Allmaras, S., 1992. A one-equation turbulence model for aerodynamic flows. AIAA Paper (92-0439)
Spalding, D.B., 1983. Chemical-reaction in turbulent fluids. Physicochemical Hydrodynamics, 4(4), 323–336.
Spalding, D.B., 1985. A turbulence model for buoyant and combusting flows. NASA STI/Recon Technical Report N, 86, 22909.
Spalding, D.B., Malin, M.R., 1984. A two-fluid model of turbulence and its application to heated plane jets and wakes. Physicochemical Hydrodynamics, 5(5), 339–361.
Thomas, L.H., 1949. Elliptic problems in linear difference equations over a network. Watson Sci. Comput. Lab. Rept., Columbia University, New York, 1, 71.
Tian, L., Ahmadi, G., 2007. Particle deposition in turbulent duct flows—comparisons of different model predictions. Journal of Aerosol Science, 38(4), 377–397.
Yen, S.C., Liu, J.H., 2011. Wake flow behind two side-by-side square cylinders. International Journal of Heat and Fluid Flow, 32(1), 41–51.
Youngs, D.L., 1965. Representation of the molecular mixing process in a two-phase flow turbulent mixing model. Proc. 5th International Workshop on Compressible Turbulent Mixing, Ed. R.Young, J.Glimm & B.Boston, ISBN 9810229100, World Scientific.
Yu, K., Ding, G., Chen, T., 2008. Modified two-fluid model for air curtains in open vertical display cabinets. International Journal of Refrigeration, 31(3), 472–482.
Zhang, H., Ahmadi, G., Fan, F.-G., McLaughlin, J.B., 2001. Ellipsoidal particles transport and deposition in turbulent channel flows. International Journal of Multiphase Flow, 27(6), 971–1009.
Zou, L., Lin, Y., Lam, K., 2008. Large-eddy simulation of flow around cylinder arrays at a subcritical Reynolds number. Journal of Hydrodynamics, 20(4), 403–413.

Received 12 April 2025
Accepted 4 December 2025